CRYSTAL GROWTH & DESIGN

pubs.acs.org/crystal

Article

Secondary Nucleation of α-Glycine Induced by Fluid Shear Investigated Using a Couette Flow Cell

Published as part of Crystal Growth & Design virtual special issue "Industrial Crystallization: ISIC 22/BACG 52".

Andrew Cashmore, Konstantinos Georgoulas, Christopher Boyle, Mei Lee, Mark D. Haw, and Jan Sefcik*

Cite This: *Cryst. Growth Des.* 2024, 24, 4975−4984

Read Online

ACCESS | Metrics & More | Article Recommendations | Supporting Information

ABSTRACT: A Couette cell flow device was designed, and an experimental procedure was developed to enable a quantitative study of the effects of fluid shear on secondary nucleation using a fixed seed crystal under controlled supersaturation, temperature, and flow conditions. This approach excludes mechanical impact, which is often considered to be the principal source of secondary nucleation, for example, through crystal attrition. We found that secondary nucleation rates of α-glycine in aqueous solutions induced by fluid shear were very significant and about 6 orders of magnitude higher than primary nucleation rates at the same conditions. Secondary nucleation rates per seed crystal were found to be about 1 order of magnitude lower compared with the magnetically stirred vials investigated previously, where a single seed crystal was freely moving, and thus, its mechanical impacts could not be ruled out. Computational fluid dynamics was used to calculate the wall shear stress along the surface of fixed seed crystals placed in the Couette cell gap at rotation rates between 100 and 600 rpm investigated here. This approach allows relating the secondary nucleation rate to the wall shear stress so that quantitative models can be developed to capture the effects of fluid shear on secondary nucleation kinetics. Such models will then facilitate scale-up and transfer of secondary nucleation kinetics between various equipment used in industrial crystallization processes.

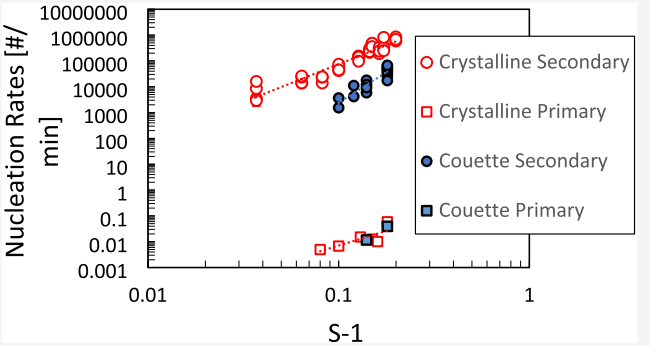

INTRODUCTION

Secondary nucleation, the formation of crystal nuclei from solution due to the presence of existing crystals, plays an important role in many industrial crystallization applications. While primary nucleation, the initial formation of crystal nuclei from solution, is a strongly stochastic process and therefore difficult to control, secondary nucleation can be controlled through the number of crystals in contact with solution and their fluid shear environment and mechanical interactions.

Despite a significant effort over many years, a fundamental understanding of secondary nucleation mechanisms remains lacking,[1−4] creating a barrier to the development of quantitative predictive models and rational crystallization process design. Mechanisms proposed in previous literature involve existing crystals giving rise to new nuclei due to either mechanical contact between crystals and agitator, vessel wall, or other crystals or the effect of fluid shear at the surface of crystals. Mechanical contact between crystal and agitator can lead to crystal attrition or breakage, which produces new crystal particles. While this is normally described in the literature as a type of secondary nucleation, it is not really a process of phase change from liquid to solid but rather a division of an existing solid phase into a more numerous number of population, as it is reflected in traditional secondary nucleation kinetic models.[5] On the other hand, mechanical contact does not necessarily lead to detachment of a solid fragment but can still facilitate a genuine phase transformation.[6] Fluid shear is often assumed to be less significant than mechanical impact,[2] but previous work has demonstrated that the importance of fluid shear on secondary nucleation and stirred tanks,[7−9] fluid jets[10] and Taylor Couette flow cells[11] has been used to investigate the effects of fluid shear on secondary nucleation.

In practice, both fluid shear and mechanical impact may take place simultaneously, while the dominant effect depends on

Received: January 29, 2024
Revised: May 23, 2024
Accepted: May 23, 2024
Published: June 10, 2024

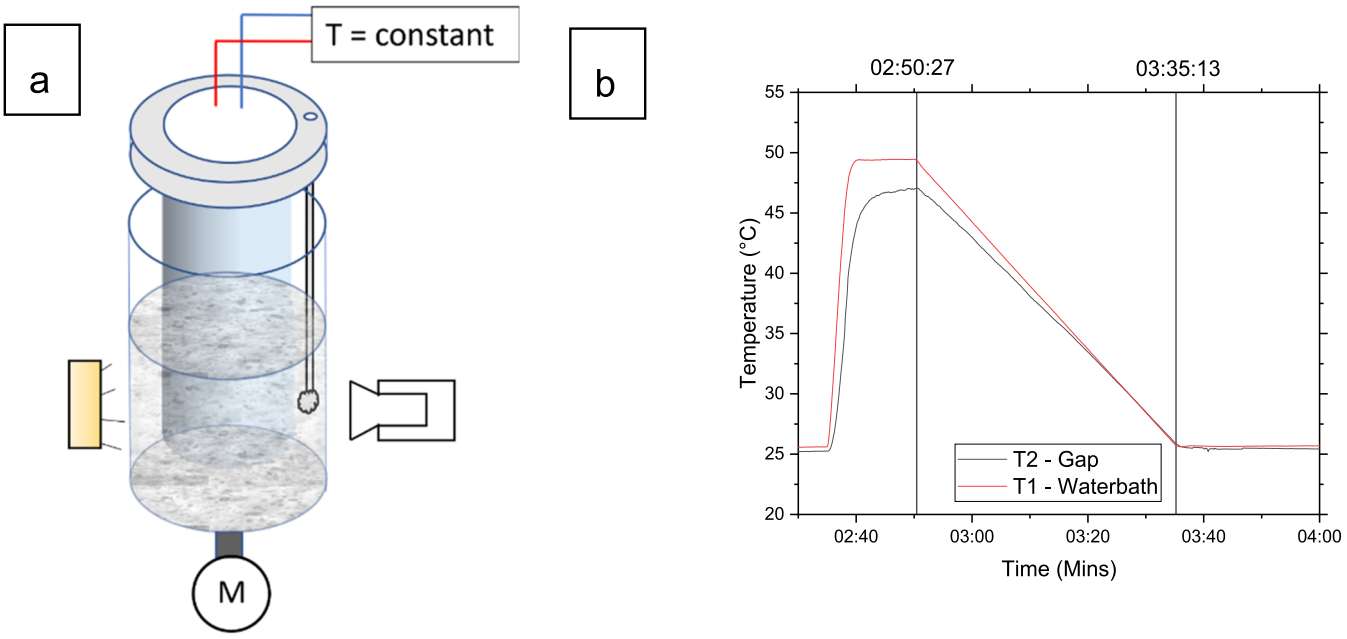

Figure 1. (a) Schematic of the Couette flow cell. The inner cylinder remains stationary, while the outer cylinder rotates and is driven by motor M. The hollow inner cylinder is filled with water supplied by an external circulating water bath. The seed is held in a fixed position at the end of a glass capillary inserted in the annular gap between the two concentric cylinders. A fixed camera and a lighting system enable imaging-based measurement of the crystal number and seed size over time. (b) Temperature control validation in the annular gap. The red line shows the circulating water temperature measured by a thermocouple placed in the inner cylinder. The black line shows the solution temperature measured by a thermocouple placed in the annular gap at the location of the seed crystal.

the process conditions, such as flow regime (laminar or turbulent) and intensity, vessel geometry, size distribution, and solid loading of suspended crystals. For example, large inertial crystals (e.g., size 1 mm, solid−liquid density difference 1 g/cm^3) have a Stokes number larger than 1 and will be likely to hit the impeller, while smaller crystals with better density match (Stokes number $\ll$1) will be much less likely to do so.

Experimental methods that isolate the effect of fluid shear from mechanical impact are thus needed to clarify under what conditions mechanical impact or fluid shear may dominate, as well as acquire secondary nucleation kinetics data, enhance our understanding of secondary nucleation mechanisms, and facilitate rational development of crystallization process design.

In this work, we use a laminar Couette cell geometry containing a single fixed seed crystal equipped with a high-resolution camera and automated image analysis to study the effect of fluid shear on secondary nucleation in isolation from mechanical impact. Using a fixed seed crystal helps to define and control the flow field around the seed crystal. We explore how primary and secondary nucleation kinetics are influenced by solution supersaturation and Couette cell rotation rate. We use computational fluid dynamics (CFD) to calculate the flow field and wall shear stress along the surface of fixed seed crystals placed in the Couette cell gap. This approach allows quantifying the secondary nucleation rate and relating it to the fluid shear experienced by the crystal. This will then facilitate scale-up and transfer of secondary nucleation kinetics due to fluid shear between various equipment used in industrial crystallization processes.

METHODS

Couette Cell. The Couette cell is composed of two concentric glass cylinders with the fluid subjected to shear in the gap between the cylinders. The outer cylinder is fixed at its base to a motor and rotated at a controlled rate, while the inner cylinder is held stationary. This arrangement creates a laminar shear flow within the gap without flow instabilities, which arise at higher rotation rates in the case of a rotating inner cylinder.[12] Under laminar flow conditions, velocity profiles and corresponding shear rates in the annular gap can be calculated analytically.[13] In the presence of the seed crystal in the annular gap, shear rates and wall shear stress at the seed crystal surface were calculated using CFD (see below).

A diagram of the in-house Couette cell setup used in this work is shown in Figure 1a. The inner radius of the outer cylinder is r_{out} = 32 mm, and the outer radius of the inner cylinder is r_{in} = 28 mm, so the annular gap between the two cylinders is 4 mm, and the surface-to-volume ratio in the annular gap is 5 cm^{-1}. The vertical gap between the bottom of the stationary inner cylinder and the rotating outer cylinder is 5 mm. The solution volume in the Couette cell is 50 mL. The liquid level is 5 cm from the bottom of the outer cylinder.

A three-dimensional (3D)-printed plastic guide ring at the top of the intracylinder gap ensures that the inner cylinder is held in the same fixed location for every experimental run. For seeded experiments, a single seed crystal is glued to the end of a glass capillary tube (Hirschmann glass capillary tube, 100 mm length, 1.5 mm outer diameter) inserted into the gap between the cylinders through a small hole in the guide ring, such that the seed is always held at the same position at the middle of the gap at the sufficient depth from the liquid level so as not to disturb the liquid meniscus. Outer cylinder rotation rate in revolutions per minute (RPM) is controlled via the motor voltage as measured on an analogue display.

To enable experiments under well-defined isothermal conditions, the hollow inner cylinder of the Couette cell is filled with water supplied by an external controlled-temperature circulating water bath, enabling the control of the gap temperature to within ±0.5 °C at the working temperature of 25 °C used here. The circulating water bath-based temperature control also enables the pretreatment of the starting solution and a repeatable cooling profile to reach the desired temperature in a controlled manner.

Temperature control was validated by placing one thermocouple in the inner cylinder and another in the annular gap between the two cylinders. The two temperatures were monitored using the PicoLog

https://doi.org/10.1021/acs.cgd.4c00130
Cryst. Growth Des. 2024, 24, 4975−4984

TC-08 and corresponding software while running the system through a typical temperature profile used in the measurements here, showing that the gap temperature closely follows the water bath temperature (see Figure 1b).

Solution Preparation and Couette Cell Filling. Glycine powder was obtained from Sigma-Aldrich (≥99% electrophoresis). For each experimental run, the mass of powder required to obtain a required solution concentration C is added to 50 mL of deionized water (milli-Q). The solution supersaturation S is then determined by the ratio of the solution concentration C to the solubility C_s of α-glycine in water at the working temperature of 25 °C, C_s = 249.5 mg/g (expressed as mg of glycine per g of water).[14] The sample is heated to 60 °C and stirred at 700 rpm using a magnetically agitated hot plate for 1 h to ensure complete dissolution of the powder. Prior to filling with the solution, the Couette cell is preheated to 40 °C using the water bath to limit the influence of cool surfaces, inducing heterogeneous nucleation. To enable filling, the inner cylinder is raised to allow the glycine solution to be poured directly from the dissolution beaker into the outer cylinder of the Couette cell. The inner cylinder is then lowered back into position. Raising and lowering the inner cylinder is achieved using a fixed stand so that the cylinder always returns to the same position within the outer cylinder. The glycine solution with a total volume of 50 mL is held for an additional 30 min at 40 °C (i.e., undersaturated) subjected to shear by rotation of the Couette outer cylinder at 50 rpm to ensure complete redissolution of any nuclei, which may have formed on solution transfer. Rotation is then stopped, and the Couette cell is cooled at a rate of 0.5 °C/min over 30 min to reach the desired experimental temperature of 25 °C.

Imaging. To monitor crystal nucleation and growth, a high-speed camera (Photron FASTCAM) and a diffuse light source (supplied with the camera for illumination) are located at the sides of the Couette cell (see Figure 1a), recording images every 5 s throughout each experiment once isothermal conditions are reached. The images are then automatically processed using an in-house image analysis algorithm to monitor the size of the growing seed crystal and to detect and count newly formed particles (from around 20 μm size upward) in recorded images. To estimate the volumetric number concentration, i.e., number density, of suspended particles from particle number counts in recorded images, a calibration was performed using suspended polystyrene spheres under identical imaging conditions. Further details of image system calibration and estimation of nucleation and growth rates from the recorded images are given below.

Unseeded Experiments and Primary Nucleation Kinetics. Unseeded experiments were carried out at one rotation rate and two different supersaturations (Table 1). Because primary nucleation is a stochastic process, a sufficient number of repetitions is required to estimate primary nucleation kinetics. It has been shown previously[15] that a number of repetitions on the order of 10 was typically sufficient to generate a meaningful probability distribution for the estimation of primary nucleation kinetics. Here, 10 repetitions were performed at S = 1.18 and 11 repetitions at S = 1.14. Each repetition results in an estimate of induction time, the time after t_0 at which nucleation of crystals is first reliably detected by the imaging system.

Plotting the induction time cumulative probability distribution $P(t)$ across the set of repetitions at the given S and fitting a relevant model then enables estimation of primary nucleation kinetics. Here, we use the model proposed by Jiang and ter Horst.[16] The model assumes that there is a constant primary nucleation rate J, defining the probability per unit volume per unit time of a primary nucleation event in the sample. Nucleation events occur independently in each repetition according to a Poisson distribution in time: it is further assumed that there is a delay between the primary nucleation event itself and the time at which crystallization is detected, designated as the growth time t_g. The growth time is assumed to be a constant (i.e., the same in all repetitions) and corresponds to the time required for the initial nucleus to grow sufficiently large to induce (unseeded) secondary nucleation, resulting in the formation of many small crystals, which are then detectable by imaging. Under these assumptions, the theoretical cumulative probability distribution can be expressed as follows:

$$P(t) = 1 - \exp(-JV(t - t_g)) \quad (1)$$

where J is the primary nucleation rate, V is the solution volume, and t_g is the growth time. The experimental cumulative probability distribution of induction times $P(t)$ across a set of repetitions is calculated as $P(t) = \frac{M^+(t)}{M}$, where M is the total number of experiments, and M^+ is the number of experiments in which nucleation was detected at a time less than or equal to t. Equation 1 is then used to fit the experimental cumulative probability distribution of induction times, taking the sample volume as 50 mL and treating both the primary nucleation rate and growth time as fitting parameters.

Seeded Experiments. For seeded experiments, the same experimental procedure for solution preparation was followed as for unseeded experiments, followed by the crystal seed insertion immediately after the desired working temperature was reached and before commencing shear at the desired rotation rate. α-Glycine seed crystals were grown using evaporative crystallization from a known initial solution concentration placed in a Petri dish and allowed to evaporate at room temperature and pressure. Crystal seeds of similar sizes and shapes (length of 2.0 ± 0.5 mm) were selected for use in seeded experiments. In each experiment, a seed is carefully glued (Loctite Precision Max) to the end of a cylindrical glass capillary tube holder (1.5 mm diameter) and then, before insertion into the Couette cell, subjected to washing to remove potential surface contaminants such as microsized crystallites or dust, which have been associated in the literature with the initial breeding mechanisms of secondary nucleation,[17,18] in order to exclude this mechanism as a possible driver of secondary nucleation. Washing involves using a syringe to flow a total volume of 15 mL of water (Milli-Q, 18.2 MΩ cm) at room temperature over the seed surface. The capillary holder with the washed seed is inserted into the guide ring, and the guide is inserted into the Couette cell such that the seed is held in a fixed position in the middle of the gap between the two concentric cylinders at a sufficient depth from the liquid level so as not to disturb the liquid meniscus. At this point, rotation of the outer cylinder is immediately commenced. The camera is positioned such that simultaneous observation of both the seed crystal held in the fixed position and newly formed crystals suspended in the bulk solution is possible. Table 1 summarizes the flow and supersaturation conditions studied in seeded experiments.

Crystal Growth Kinetics. Crystal growth kinetics are studied in the Couette cell by measuring the growth of the seed crystal using an in-house developed image analysis technique. At the start of each seeded experiment, the camera is placed such as to ensure that the

Table 1. Details of Experimental Runs[a]

rotation rate (RPM)	empty gap shear rate (s^{-1})	cylinder wall shear stress (Pa)	supersaturation	
			seeded experiments	unseeded experiments
100	84	0.084	1.10, 1.14, 1.18	
200	168	0.168	1.10, 1.12, 1.14, 1.18	1.14, 1.18
300	251	0.251	1.10	
400	335	0.335	1.10, 1.14, 1.18	
600	503	0.503	1.14, 1.18	

[a]Outer cylinder rotation rates, corresponding empty gap shear rates (with gap size 4 mm), and cylinder wall shear stress calculated using a liquid viscosity of 0.001 Pa·s, and supersaturation values S used in seeded (secondary nucleation) and unseeded (primary nucleation) experiments.

https://doi.org/10.1021/acs.cgd.4c00130
Cryst. Growth Des. 2024, 24, 4975−4984

seed crystal occupies a small portion of the image frame with all its edges visible. During experiments, images are taken every 5 s. For seed crystal size measurement, an algorithm was developed to identify the outline edge of the seed crystal and thus generate an enclosed projected surface area (A). The surface area was converted to an effective crystal size $L = A^{1/2}$, and the growth rate was estimated from the slope of a dependence of L on time elapsed since the start of the outer cylinder rotation.

Secondary Nucleation Kinetics. Secondary nucleation is revealed by the appearance of new suspended particles that are transported around the cell by the circular flow. The image analysis algorithm detects particles in an image at a given time via the same edge-detection method as for seed crystal growth measurement, and outputs provide a count of particles for each image. Furthermore, a calibration is required to obtain a conversion factor between the particle number N counted in the image and the particle number density in the sample volume (N_ρ). Calibration was performed by imaging polystyrene microspheres (EPRUI Nanoparticles & Microspheres Co) of diameter 50 μm and density 1050 mg/mL at a range of known volumetric concentrations in the Couette cell using imaging conditions identical to those used in the crystallization experiments. The PS suspension volumetric number density N_p is calculated by dividing the known mass concentration C_p by the product of the particle density and the sphere volume based on the quoted sphere size.

In a typical secondary nucleation experiment, there is a delay time between the insertion of the seed crystal and the appearance of newly formed crystals, as there needs to be a sufficient number of crystals with sufficient size for them to be detected over and above the background noise in recorded images.[19] Once the average number of crystals detected in images exceeds the background count, there is a steady increase of the number count until the image saturates, after which the image analysis is not able to provide reliable estimates of the particle number in recorded images. The secondary nucleation rate is then estimated from the slope of the time dependence of the crystal number density once it starts increasing rapidly but is within the range of the calibration validity.

Computational Fluid Dynamics. A detailed examination of the flow field around the seed crystal was obtained through CFD modeling, which allows relating the rotation rate to wall shear stress conditions at the seed crystal surface. In order to study the effects of the fluid flow in a Couette cell on a solid crystal seed, CFD methodology was applied in a three-dimensional domain. The crystal seed was represented by two alternative object shapes: a cube or a sphere with an edge or diameter of 2 mm, respectively, while the Couette cell was simulated as a 4 mm gap between two concentric cylinders of radii equal to 28 and 32 mm. The inner wall was stationary, and the outer one was rotating at rates between 100 and 600 rpm. In all cases, the working fluid was assumed to be water with a density equal to 1000 kg/m^3 and viscosity equal to 0.001 Pa·s.

ANSYS Fluent was used to perform numerical investigations solving the continuity and momentum conservation equations for an incompressible Newtonian fluid flow. The flow in the numerical domain is purely laminar in the absence of the crystal seed for any rotation rate that was used in this work. The introduction of the seed crystal in the Couette cell gap resulted in more disturbed flows, and at higher Reynolds numbers, the introduction of a turbulence model was essential; otherwise, the numerical instabilities that occurred resulted in unrealistic flow patterns. The shear stress transport (SST) k–ω model[20] was used as it is a powerful approach that blends the robust near-wall formulation of the traditional k–ω model with the free-stream independence of the k–ε model in the far field. A blending function is used to couple the standard k–ω and transformed k–ε models in a way that activates the k–ω model in near-wall regions or the k–ε model in regions away from the wall.

In laminar flow conditions, the wall shear stress is defined as the product of the dynamic viscosity of the fluid and the normal velocity gradient at the wall. For no-slip wall conditions, the properties of the flow adjacent to the wall are used. When using the SST k–ω model, the turbulent viscosity was calculated from the following equation:

$$\mu_T = \frac{\rho k}{\omega} \frac{1}{\max\left[\frac{1}{a^*}, \frac{SF_2}{a_1\omega}\right]}$$

where ρ is the density, k is the turbulent kinetic energy, ω is the specific turbulence dissipation rate, S is the strain rate, a is a coefficient that damps the turbulent viscosity to create a low-Reynolds-number correction, and F_2 is a blending function as the following:

$$F_2 = \tanh(\Phi_2^2)$$

$$\Phi_2^2 = \max\left[2\frac{\sqrt{k}}{0.09\omega y}, \frac{500\mu}{\rho y^2 \omega}\right]$$

where y is the distance to the next surface. The wall shear stress in turbulent flow can then be calculated by multiplying the turbulent viscosity with the normal velocity gradient at the wall.

RESULTS AND DISCUSSION

Unseeded Experiments: Primary Nucleation Kinetics. Primary nucleation kinetics in the Couette cell was investigated by recording isothermal induction times distributions from repeated unseeded experiments at two different supersaturations and a fixed rotation rate. Cumulative probability distributions of induction times obtained from unseeded experiments in the Couette cell at a rotation rate of 200 rpm at two different supersaturations are shown in Figure 2.

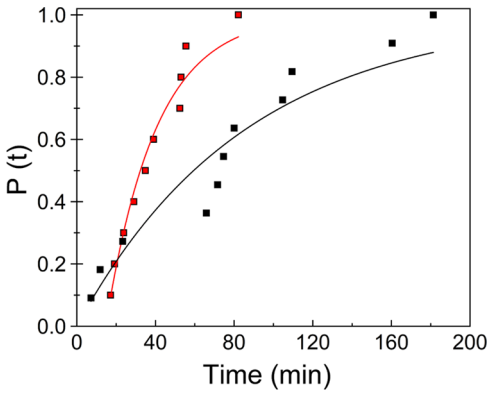

Figure 2. Cumulative probability distributions of induction times from unseeded Couette cell experiments at a rotation rate of 200 rpm. The total number of experimental repetitions was 11 and 10 for S = 1.14 (black squares) and S = 1.18 (red squares), respectively. Lines show fits of eq 1 to $P(t)$ to obtain nucleation rate J and growth time t_g (see Table 2).

Previous nucleation kinetics studies[21] used monitoring methods such as cloud point detection using transmission or imaging techniques[13] suitable for induction time measurements or particle counting approaches based on in situ imaging[22] or observation of the total number of particles obtained at the end of the experiment.[11] In this work, we use imaging for both induction time measurements in unseeded experiments and secondary nucleation kinetics measurements in seeded experiments based on in situ particle counting. It is important to note that observations obtained by both induction time and particle counting approaches depend on the interplay of primary and secondary nucleation and crystal growth kinetics, and their interpretation depends on the relative magnitude of primary and secondary nucleation kinetics.[19] In order to detect the induction time in unseeded

https://doi.org/10.1021/acs.cgd.4c00130
Cryst. Growth Des. 2024, 24, 4975−4984

experiments, a crystal needs to nucleate via primary nucleation, and then it needs to grow to a sufficient size so that it triggers secondary nucleation, which will generate a sufficient number of further crystals which can be detected. This scenario is typical for agitated systems where the initially nucleated crystal is exposed to fluid shear or mechanical contact, and secondary nucleation rates are much higher than primary nucleation rates[23] once the initial crystal becomes large enough. For example, in our previous studies of glycine nucleation, it was estimated that the initial crystal needed to grow to at least 100 μm to induce significant secondary nucleation, and crystals produced through secondary nucleation needed to grow to about 10 μm in order to be detected, using magnetically agitated vials in the crystalline setup.[19]

Under the relevant assumptions discussed in the Methods section, the theoretical distribution of induction times can be fitted to the experimental induction time data to estimate corresponding primary nucleation rates (J) and growth times (t_g), see Table 2. Please note that the standard errors indicated

Table 2. Estimated Primary Nucleation Rate J and Growth Time t_g for Glycine Aqueous Solutions in Couette Cell at a Rotation Rate of 200 rpm[a]

supersaturation, S	1.14	1.18
J [#/mL/min]	2.3×10^{-4} ($\pm 3 \times 10^{-5}$)	7.9×10^{-4} ($\pm 7 \times 10^{-5}$)
t_g [min]	0 ($\pm$6)	15 ($\pm$2)

[a]The solution volume was 50 mL. All experiments nucleated.

in Table 2 are due to fitting the specific data set with the theoretical probability distributions. While limited data sets such as those collected here are adequate to provide meaningful estimates of the primary nucleation rate, there may be significant uncertainty on the order of 50% due to the stochastic nature of the underlying nucleation process.[15] However, our aim here is to estimate an order of magnitude of primary nucleation rates from unseeded experiments using the distributions of induction time to provide a comparison with previous literature and with estimated secondary nucleation rates determined here from single crystal seeding experiments. Regarding the growth time, it would be expected to decrease with supersaturation, but it is again subject to significant uncertainty due to the stochastic nature of the underlying nucleation process. Please note that we do not use the estimated growth times reported in Table 2 in further analysis or discussion in this work.

The primary nucleation rates (per unit volume of solution) previously reported in this system for magnetically agitated vials at 700 rpm with a solution volume of 3 mL[19] are about 20−40 times higher than those obtained here at corresponding supersaturations and temperature using laminar Couette flow at 200 rpm with a solution volume of 50 mL. These values can also be compared with those previously reported for laminar Couette flow with similar shear rates and surface-to-volume ratios,[24] which were about 20−100 times higher but at a significantly higher supersaturation (S = 1.4). These results are consistent with previous observations that overall primary nucleation rates (per vessel) JV at given supersaturation and temperature can be expected to depend not only on solution volume V but also on the solution agitation and resulting fluid shear,[13,25−27] as well as solution interfacial area and materials of construction involved.[24,28,29]

We can also see that the characteristic times of primary nucleation kinetics under conditions investigated here, which can be expressed as $1/JV$, are 87 and 25 min for S = 1.14 and 1.18, respectively, and as will be seen below, the primary nucleation kinetics is therefore much slower than the secondary nucleation kinetics under these conditions.

Seeded Experiments: Crystal Growth Kinetics. Crystal growth rates were estimated from data obtained in the seeded experiments by determining the change in the effective size of the seed crystal for a range of supersaturations at a fixed rotation rate. For each experimental condition, the effective size of the seed crystal L was plotted as a function of time, and the crystal growth rate was estimated from the slope of L vs time as shown in Figure 3.

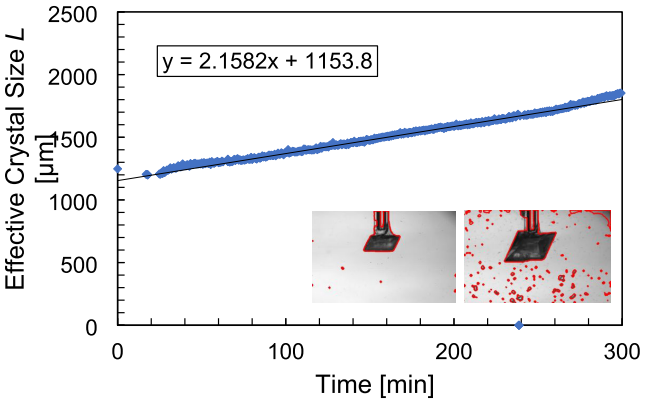

Figure 3. Example of a seed crystal size vs time used to determine the crystal growth rate. The left-hand image is at an early time, and the right-hand image is near the end of the experiment.

Crystal growth rates measured at 200 rpm at supersaturations between 1.10 and 1.18 are shown in Figure 4.

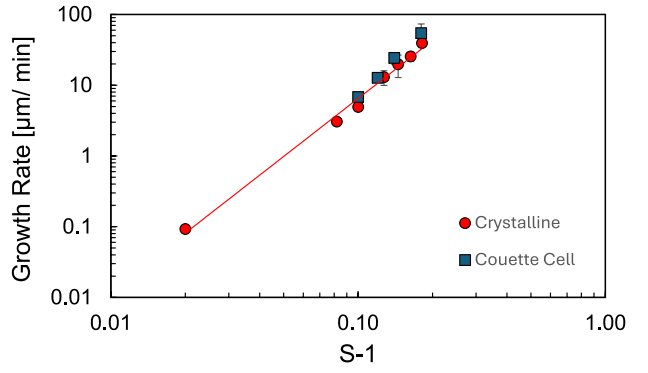

Figure 4. Crystal growth rates of α-glycine in water were measured using the Couette flow cell at a rotation rate of 200 rpm and supersaturations S = 1.10, 1.12, 1.14, and 1.18 (blue squares, each point represents a single experiment) shown together with crystal growth rates obtained previously (red circles) using vials magnetically agitated at 700 rpm.[19]

The crystal growth rate values based on measuring the crystal seed in the Couette cell are in overall good agreement with the previously measured values using magnetically agitated vials and other methodologies and flow conditions as summarized by Cashmore et al.[19]

https://doi.org/10.1021/acs.cgd.4c00130
Cryst. Growth Des. 2024, 24, 4975−4984

It appears that flow conditions do not have a significant effect on crystal growth, as expected if growth is not rate-limited by diffusion. However, there is a significant variation in the α-glycine crystal growth rate observed between individual single seed crystals, also known as the growth rate dispersion, consistent with observations in previous literature.[30] In comparison, flow conditions do not appear to have a systematic effect on the crystal growth rate, which indicates that α-glycine crystal growth is not subject to significant transport limitations in the range of supersaturations investigated here.

Seeded Experiments: Secondary Nucleation Kinetics. Secondary nucleation kinetics was investigated using seeded experiments where the number density of crystals produced following an introduction of a single seed crystal was monitored as a function of time at several values of solution supersaturation and rotation rates. To determine the crystal number density from images obtained, a calibration was performed, as described in the Methods section. Figure 5 shows the calibration relationship between the average particle number in images and the number density of particles across the range of calibration suspension concentrations.

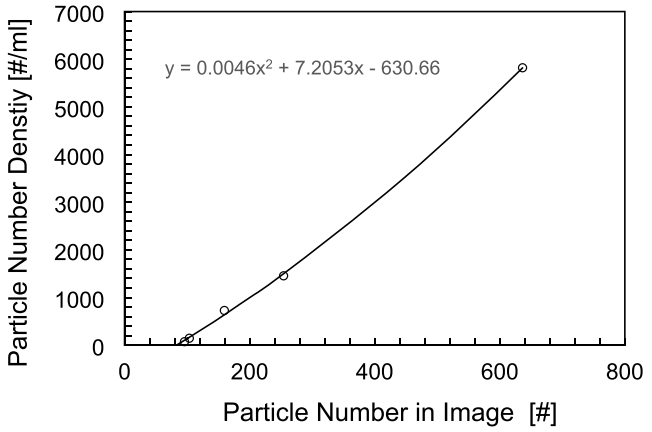

Figure 5. Calibration of particle number density based on the measured particle number count in images.

We fit a second-order polynomial to these data to obtain a calibration equation relating the average particle number count in images N and the volumetric number density N_ρ:

$$N_\rho = 0.0046N^2 + 7.2053N - 630.66 \quad (3)$$

As images contain some background features that are detected as relevant objects and thus counted as particles, there are nonzero particle number counts at zero particle number density. These are treated as the background contribution by using the calibration relationship above.

In Figure 6, we show images of particles produced through secondary nucleation in the seed crystal presence. Identified particles are indicated by red boundaries drawn around each object, and the particle number count in images N is recorded as a function of time. The corresponding particle number density N_ρ as a function of time is determined using the calibration equation (eq 3).

Similarly to our previous work using magnetically agitated vials,[19] there are uniform background fluctuations during the delay time from the beginning of the shear due to the outer cylinder rotation until the crystals produced by secondary nucleation become detectable. Afterward, the number density of crystals begins to rise steeply, and the secondary nucleation rate is estimated from a linear fit to the time dependence of the crystal number density as explained in the Methods section. Secondary nucleation kinetics was investigated using seeded experiments at supersaturations between 1.10 and 1.18 and rotation rates between 100 and 600 rpm, see Figure 7.

Secondary nucleation rates show variability of up to an order of magnitude when repeated with different seed crystals at the same experimental conditions, similar to previous observations in magnetically stirred vials.[19] The secondary nucleation rate is increasing with supersaturation as expected, although the dependence on supersaturation becomes less prominent with an increasing rotation rate. At the lowest supersaturation (S = 1.10), there is an apparent overall increase of secondary nucleation rates with rotation rates, and a power law dependence of the secondary nucleation rate B on the rotation rate r, $B = ar^b$, can be fitted (at the significance level α = 0.10) with a power law exponent close to 1 over the range of rotation rates investigated here, as shown in Figure 7. This is consistent with experimental observations that the secondary nucleation rate is negligible under quiescent conditions (when r = 0 rpm). However, it can be seen in Figure 7 that at higher supersaturations (S = 1.14 and 1.18), there is no apparent dependence of the secondary nucleation rate on the rotation rate over the range of conditions investigated here. In order to provide further insight into the effects of fluid shear on secondary nucleation kinetics observed here, we also need to understand the fluid flow field around the seed crystal held in the annular gap as a function of the Couette cell rotation rate.

Effects of Fluid Flow on Secondary Nucleation Kinetics. We quantified fluid flow effects on the crystal seed using CFD calculations to obtain the shear stress across the seed crystal surface. The CFD results are presented in Table 3 in terms of the average wall shear stress across the surface of the seed crystal held in a fixed position in the middle of the Couette cell gap. To assess the effect of the crystal shape, two different seed crystal shapes were considered, cubic and spherical, with an edge and diameter of 2 mm, respectively, where the spherical shape results in the average wall shear stress about 50% higher than that for the cubic shape. It is important to note that in both cases, the wall shear stress is distributed unequally over the seed crystal surface, where corresponding cumulative probability distributions are spanning over 2 orders of magnitude (see Figure S1 in the Supporting Information), so that maximum wall shear stress experienced at some seed crystal locations can be more than an order of magnitude higher than the average value.

In order to further understand the wall shear stress acting on the crystal seed in the Couette cell, the simulations were run with both laminar and turbulent CFD modeling to calculate the average wall shear stress acting on the cubic seed crystal. While laminar models become less accurate when flows develop instabilities at higher RPM, using turbulence models for laminar flows can lead to incorrect results due to the artificial turbulent viscosity they introduce. Therefore, the SST $k-\omega$ model was used, where the turbulent viscosity approaches zero when the turbulent kinetic energy is zero, allowing meaningful comparisons to the laminar model. While both laminar and turbulent models produced very similar results at the lowest rotation rates, afterward, the results diverged as the flow was no longer purely laminar, and it can be seen that the laminar model underpredicts the total wall shear stress

https://doi.org/10.1021/acs.cgd.4c00130
Cryst. Growth Des. 2024, 24, 4975−4984

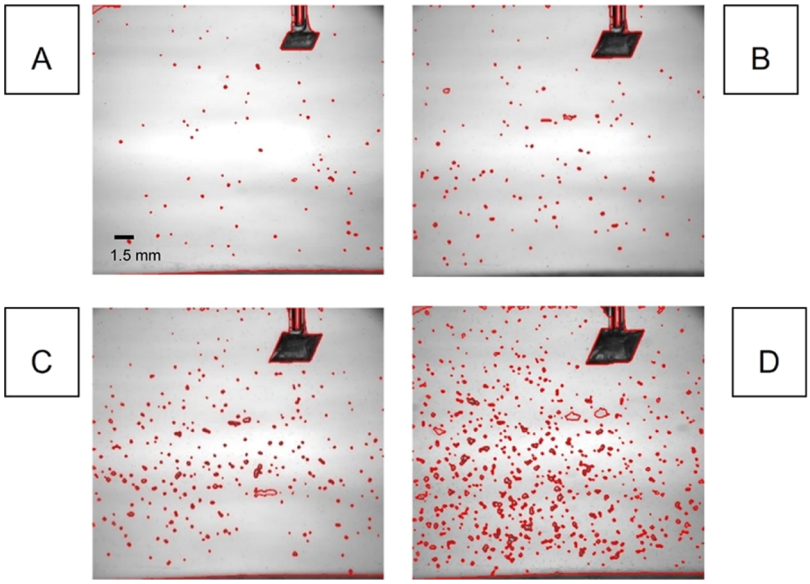

Figure 6. Example images showing the progression over time (A–D) of a secondary nucleation experiment in the Couette flow cell. The seed crystal attached to the end of a glass capillary can be seen at the top of the image, while the red lines around the small objects throughout the images show the boundaries of new crystals as identified by the image analysis algorithm.

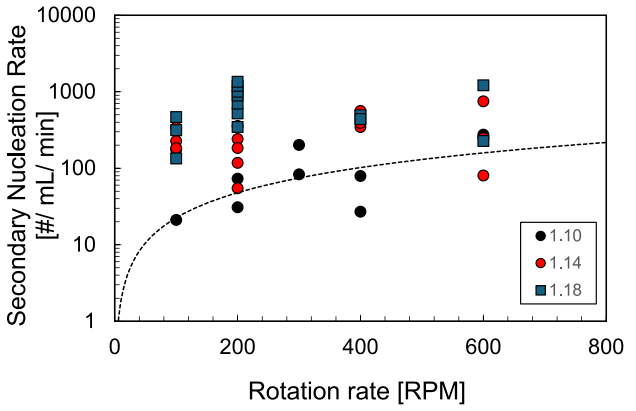

Figure 7. Secondary nucleation rate dependence on the rotation rate for supersaturations S = 1.10 (black circles), S = 1.14 (red circles), and S = 1.18 (blue squares). The line shows power law relationships between the secondary nucleation rate and rotation rate for the lowest supersaturation S = 1.10.

Table 3. Average Wall Shear Stress across Crystal Seed Surface at Different Rotation Rates Calculated Using CFD for Two Different Seed Crystal Shapes (Cubic and Spherical)

rotation rate (RPM)	average wall shear stress across cubic seed surface (Pa)	average wall shear stress across spherical seed surface (Pa)
100	0.91	1.44
200	2.21	3.25
300	3.54	6.52
400	4.62	8.29
600	9.51	12.1

compared to the SST $k-\omega$ model (Table S1). The Reynolds shear stress was calculated using the SST $k-\omega$ model, but it can be seen in Table S1 that it only contributes less than 1% of the overall wall shear stress at 600 rpm, which was the maximum rotation rate used here. We can therefore conclude that while nonlaminar flow effects become significant at higher RPM conditions, Reynolds stresses make only a small contribution to the overall wall shear stress experienced at the seed crystal surface in the Couette cell used here. At the same time, the fluid flow remains laminar in the Couette cell gap, which is far away from the crystal seed.

We now compare secondary nucleation rates measured here using a fixed seed crystal under laminar fluid shear in the Couette cell at 200 rpm with secondary nucleation rates from previous experiments, where a freely moving seed crystal was inserted into a magnetically agitated vial.[19] We can also compare primary nucleation rates measured here in unseeded experiments under laminar fluid shear in the Couette cell at 200 rpm with those previously measured in magnetically agitated vials.[19] In Figure 8, we show relevant nucleation rates per vessel (BV and JV for secondary and primary nucleation, respectively) rather than per unit volume as a function of solution supersaturation (all experiments were at the same temperature). In both cases, primary nucleation rates were around 6 orders of magnitude slower than secondary nucleation, which shows that particle counting is suitable for quantifying secondary nucleation rates but not primary nucleation rates under the conditions considered here, as discussed above.

As we can see from Figure 8, laminar fluid flow in the Couette cell using a single seed crystal held at a fixed position induces secondary nucleation rates (per single seed crystal in a vessel) around an order of magnitude lower than observed in the magnetically agitated vials containing a single freely moving seed crystal. While the flow field effect on a freely moving crystal under magnetically agitated conditions is difficult to quantify, there will be the additional role of turbulent stresses,[8] which constitute a negligible contribution to the overall shear stress in the Couette cell at 200 rpm but may be significant under magnetic agitation conditions. Furthermore, observations indicated that the seed crystal tended to remain near the base of the magnetically stirred vial in the proximity of the stirrer bar in our previously reported experiments.[19] Therefore,

https://doi.org/10.1021/acs.cgd.4c00130
Cryst. Growth Des. 2024, 24, 4975−4984

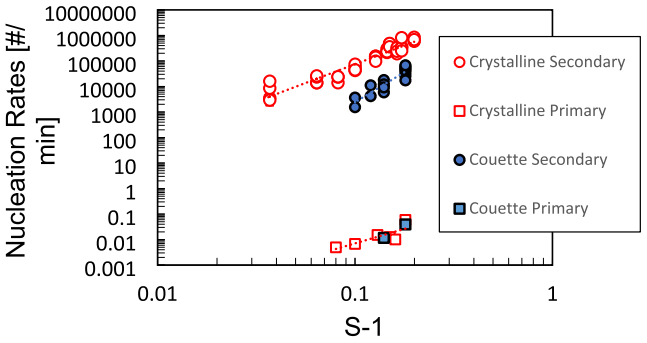

Figure 8. Primary and secondary nucleation rates under different flow conditions: comparison of Couette cell (V = 50 mL) at 200 rpm with magnetically agitated vials (V = 3 mL) at 700 rpm. Secondary nucleation rates per vessel (BV) for the Couette cell are with a single fixed seed crystal (blue circles) and for magnetically agitated vials are with a single freely moving seed crystal (red circles). Each point was averaged across 2−7 repeats. Error bars are shown for values with a minimum of three repeats, although they are smaller than the symbol size in most cases. Also shown are primary nucleation rates per vessel (JV) for the Couette cell (blue squares) and magnetically agitated vials (red squares).

mechanical impacts on the freely moving seed crystal from the magnetic stirrer or vial walls cannot be excluded, and these can also be expected to contribute to the overall secondary nucleation rate observed in the magnetically agitated vials. In contrast, the crystal seed held in a fixed position in the Couette cell gap allows us to avoid any mechanical impact so that the effects of fluid shear are studied in isolation from the effects of mechanical impact.

Role of Fluid Shear in Secondary Nucleation. Results presented and discussed above show that fluid shear induces secondary nucleation of glycine in aqueous solutions without any mechanical impact on or contact with the α-glycine seed crystal. These results are consistent with previous literature where the fluid shear was found to induce secondary nucleation in other systems, including magnesium sulfate,[9,31] citric acid,[11] sucrose,[32] and potassium alum[10] in aqueous solutions, ε-caprolactam in toluene,[33] and paracetamol in isopropanol.[8] In all of these works, great care was taken to rule out secondary nucleation induced through mechanical contact by using seed crystals held in fixed positions within surrounding fluid flows. It is also important to rule out so-called initial breeding, where small crystalline particles attached to a large seed crystal are introduced into the system by careful seed preparation procedures, as implemented here and highlighted in previously published works. As discussed above, primary nucleation rates estimated from induction time distributions are often found to be several orders of magnitude lower than secondary nucleation rates under the same flow conditions. It is interesting to note that both primary and secondary nucleation rates are induced by fluid shear, with much longer induction times and negligible secondary nucleation rates observed in quiescent systems compared to agitated ones.

We would also like to comment on what the role of fluid shear on secondary nucleation is likely to be under typical crystallization conditions and what are possible underlying mechanisms. When one inspects widely used books dealing with industrial crystallization[34,35] and review papers dealing with secondary nucleation, fluid shear is often mentioned among secondary nucleation mechanisms, in addition to initial breeding, dendritic, and attrition mechanisms, which are based on mechanical separation of parts of existing crystals and do not involve an actual phase transformation inherent to crystal nucleation. In typical crystallization processes, crystals are suspended and move around due to agitation, so it is not straightforward to isolate the effects of fluid shear mechanical impact on the overall secondary nucleation kinetics. It is however possible to assess the likelihood of crystal collisions using dimensionless number considerations based on corresponding Stokes (St) or Reynolds (Re) numbers[36,37] or using multiphase CFD approaches. Based on these approaches, larger, heavier particles, such as inorganics with particle sizes on the order of 1 mm, which do not follow fluid streamlines due to significant inertial effects ($St > 1$), are likely to be subject to mechanical impacts. However, smaller, lighter particles, such as organics with sizes on the order 0.1 mm, typical for pharmaceutical and fine chemicals manufacturing, with $St \ll 1$, are likely to follow fluid streamlines and avoid mechanical collisions. Furthermore, organic molecular crystals are often softer and more elastic, in contrast with harder, more brittle inorganic ionic and/or covalent crystals, and so, they may be less likely to undergo attrition or breakage. Thus, it can be expected that fluid shear-induced secondary nucleation may be significant under typical crystallization conditions for many systems of interest, and so, it is crucial to be able to quantify the corresponding secondary nucleation kinetics and develop appropriate population balance models appropriately reflecting underlying physical phenomena.

There have been several plausible mechanisms proposed in previous literature trying to explain the effects of fluid shear on secondary nucleation. These generally include solute clustering in the solution region adjacent to the surface of a growing seed crystal, resulting in the formation of viable crystal nuclei in this interfacial region.[38−40] These are then carried away by fluid flow, which results in the formation of new crystals away from the seed crystal. Fluid flow can also perhaps facilitate convective transport of clusters or subcritical nuclei from bulk solution toward the interfacial layer, where they can be stabilized into viable nuclei[40] and then carried away from the growing crystal surface. Both of these effects can of course be facilitated by mechanical contact, so mechanical impact-induced secondary nucleation does not necessarily need to involve attrition either.[6] On the other hand, in the absence of fluid flow, such clusters are only subject to Brownian motion, and due to their size, they would be unlikely to escape from the interfacial layer before getting incorporated into the growing crystal so that there would be negligible secondary nucleation in quiescent systems.

CONCLUSIONS

A Couette flow cell was designed, and an experimental procedure was developed to enable the measurement of secondary nucleation kinetics using a fixed seed crystal under controlled flow conditions. This approach enables the isolation of the fluid shear effect on secondary nucleation, excluding other effects such as mechanical impact or initial breeding. Experiments were conducted to evaluate the effect of the rotation rate of the Couette outer cylinder and solution supersaturation on the kinetics of secondary nucleation and seed growth rate under isothermal conditions. Primary nucleation kinetics was also measured in the absence of the seed crystal. The secondary nucleation rates were about 6 orders of magnitude higher than the primary nucleation rates

https://doi.org/10.1021/acs.cgd.4c00130
Cryst. Growth Des. 2024, 24, 4975−4984

under the same flow conditions, which was a similar observation as those made previously for magnetically stirred vials. The secondary nucleation rate per single seed crystal was about an order of magnitude lower than that observed in magnetically stirred vials with freely moving seed crystals at corresponding supersaturation. This clearly shows that the secondary nucleation induced by fluid shear plays a significant role in this crystallization process under the conditions examined here. There was a dependence of the secondary nucleation rate on the rotation rate observed at the lowest supersaturation investigated here, although there was no apparent dependence at higher supersaturations. Using CFD, we showed that the flow field in the presence of a seed crystal was the Couette cell gap that was laminar until 200 rpm and became increasingly unstable at higher rotation rates, although it was always laminar in the empty gap as the outer cylinder was rotating. We also used CFD to calculate wall shear stress distributions and corresponding averages across seed crystal surfaces as a function of flow conditions in order to relate the observed secondary nucleation rates to flow conditions. This approach can be used to assess the sensitivity of secondary nucleation to flow conditions anticipated in crystallization process development and to facilitate the development of quantitative models for fluid shear-induced secondary nucleation kinetics for population balance modeling.

■ ASSOCIATED CONTENT

Supporting Information

The Supporting Information is available free of charge at https://pubs.acs.org/doi/10.1021/acs.cgd.4c00130.

Details of the fluid flow fields around the seed crystal and wall shear stresses across the seed crystal surface (PDF)

■ AUTHOR INFORMATION

Corresponding Author

Jan Sefcik − *EPSRC Future Manufacturing Hub in Continuous Manufacturing and Advanced Crystallisation (CMAC), Technology and Innovation Centre, University of Strathclyde, Glasgow G1 1RD, U.K.; Department of Chemical and Process Engineering, University of Strathclyde, Glasgow G1 1XJ, U.K.*; Email: jan.sefcik@strath.ac.uk

Authors

Andrew Cashmore − *EPSRC Future Manufacturing Hub in Continuous Manufacturing and Advanced Crystallisation (CMAC), Technology and Innovation Centre, University of Strathclyde, Glasgow G1 1RD, U.K.; Department of Chemical and Process Engineering, University of Strathclyde, Glasgow G1 1XJ, U.K.*; orcid.org/0000-0001-8449-5300

Konstantinos Georgoulas − *Department of Chemical and Process Engineering, University of Strathclyde, Glasgow G1 1XJ, U.K.*

Christopher Boyle − *EPSRC Future Manufacturing Hub in Continuous Manufacturing and Advanced Crystallisation (CMAC), Technology and Innovation Centre, University of Strathclyde, Glasgow G1 1RD, U.K.; Department of Chemical and Process Engineering, University of Strathclyde, Glasgow G1 1XJ, U.K.*

Mei Lee − *GSK plc, Stevenage SG1 2NY, U.K.*

Mark D. Haw − *Department of Chemical and Process Engineering, University of Strathclyde, Glasgow G1 1XJ, U.K.*

Complete contact information is available at: https://pubs.acs.org/10.1021/acs.cgd.4c00130

Notes

The authors declare no competing financial interest.

■ ACKNOWLEDGMENTS

The authors would like to acknowledge that this work was carried out in the CMAC National Facility housed within the University of Strathclyde's Technology Innovation Centre and funded with a UKRPIF (UK Research Partnership Institute Fund) capital award (Grant ref: HH13054) from the Higher Education Funding Council for England (HEFCE). We would like to acknowledge funding from EPSRC Continuous Manufacturing and Advanced Crystallization Future Manufacturing Research Hub (Grant ref: EP/P006965/1) and from GSK.

■ REFERENCES

(1) Xu, S.; Hou, Z.; Chuai, X.; Wang, Y. Overview of Secondary Nucleation: From Fundamentals to Application. *Ind. Eng. Chem. Res.* **2020**, *59*, 18335−18356.

(2) Agrawal, S. G.; Paterson, A. H. J. Secondary Nucleation: Mechanisms and Models Secondary Nucleation: Mechanisms and Models. *Chem. Eng. Commun.* **2015**, *202* (5), 698−706.

(3) Zhang, D.; Wang, X.; Ulrich, J.; Tang, W.; Xu, S.; Li, Z.; Rohani, S.; Gong, J. Control of Crystal Properties in a Mixed-Suspension Mixed-Product Removal Crystallizer: General Methods and the Effects of Secondary Nucleation. *Cryst. Growth Des.* **2019**, *19*, 3070−3084.

(4) Garside, J.; Rusli, I. T.; Larson, M. A. Origin and Size Distribution of Secondary Nuclei. *AIChE J.* **1979**, *25* (1), 57−64.

(5) Mersmann, A.; Sangl, R.; Kind, M.; Pohlisch, J. Attrition and secondary nucleation in crystallizers. *Chem. Eng. Technol.* **1988**, *11* (1), 80−88.

(6) Cui, Y.; Myerson, A. S. Experimental Evaluation of Contact Secondary Nucleation Mechanisms. *Cryst. Growth Des.* **2014**, *14*, 5152−5157.

(7) Yousuf, M.; Frawley, P. J. Secondary Nucleation from Nuclei Breeding and Its Quantitative Link with Fluid Shear Stress in Mixing: A Potential Approach for Precise Scale-up in Industrial Crystallization. *Org. Process Res. Dev.* **2019**, *23*, 926−934.

(8) Yousuf, M.; Frawley, P. J. Experimental Evaluation of Fluid Shear Stress Impact on Secondary Nucleation in a Solution Crystallization of Paracetamol. *Cryst. Growth Des.* **2018**, *18*, 6843−6852.

(9) Sung, C. Y.; Estrin, J.; Youngquist, G. R. Secondary Nucleation of Magnesium Sulfate by Fluid Shear. *AIChE J.* **1973**, *19* (5), 957−962.

(10) Tai, C. Y.; Tai, C. D.; Chang, M. H. Effect of Interfacial Supersaturation on Secondary Nucleation. *J. Taiwan Inst. Chem. Eng.* **2009**, *40*, 439−442.

(11) Wang, M.-L.; Huang, H.-T.; Estrin, J. Secondary Nucleation of Citric Acid Due to Fluid Forces in a Couette Flow Crystallizer. *AIChE J.* **1981**, *27* (2), 312−315.

(12) Andereck, C. D.; Liu, S. S.; Swinney, H. L. Flow Regimes in a Circular Couette System with Independently Rotating Cylinders. *J. Fluid Mech.* **1986**, *164*, 155−183.

(13) Forsyth, C.; Mulheran, P. A.; Forsyth, C.; Haw, M. D.; Burns, I. S.; Sefcik, J. Influence of Controlled Fluid Shear on Nucleation Rates in Glycine Aqueous Solutions. *Cryst. Growth Des.* **2015**, *15*, 94−102.

(14) Rowland, D. Thermodynamic Properties of the Glycine + H2O System. *J. Phys. Chem. Ref. Data* **2018**, *47*, No. 023104.

(15) Yerdelen, S.; Yang, Y.; Quon, J. L.; Papageorgiou, C. D.; Mitchell, C.; Houson, I.; Sefcik, J.; ter Horst, J. H.; Florence, A. J.; Brown, C. J. Machine Learning-Derived Correlations for Scale-Up and Technology Transfer of Primary Nucleation Kinetics. *Cryst. Growth Des.* **2023**, *23* (2), 681−693.

(16) Jiang, S.; ter Horst, J. H. Crystal Nucleation Rates from Probability Distributions of Induction Times. *Cryst. Growth Des.* **2011**, *11* (1), 256−261.
(17) Steendam, R. R. E.; Frawley, P. J. Secondary Nucleation of Sodium Chlorate: The Role of Initial Breeding. *Cryst. Growth Des.* **2019**, *19* (6), 3453−3460.
(18) *Handbook of Industrial Crystallization*; Myerson, A. S.; Erdemir, D.; Lee, A. Y., Eds.; Cambridge University Press, 2019.
(19) Cashmore, A.; Miller, R.; Jolliffe, H.; Brown, C. J.; Lee, M.; Haw, M. D.; Sefcik, J. Rapid Assessment of Crystal Nucleation and Growth Kinetics: Comparison of Seeded and Unseeded Experiments. *Cryst. Growth Des.* **2023**, *23* (7), 4779−4790.
(20) Menter, F. R. Two-Equation Eddy-Viscosity Turbulence Models for Engineering Applications. *AIAA J.* **1994**, *32* (8), 1598−1605.
(21) Devos, C.; Gerven, T. V.; Kuhn, S. A Review of Experimental Methods for Nucleation Rate Determination in Large-Volume Batch and Micro Fluidic Crystallization. *Cryst. Growth Des.* **2021**, *21* (4), 2541−2565.
(22) Briuglia, M. L.; Sefcik, J.; ter Horst, J. Measuring Secondary Nucleation through Single Crystal Seeding. *Cryst. Growth Des.* **2019**, *19*, 421−429.
(23) Hoffmann, J.; Flannigan, J.; Cashmore, A.; Briuglia, M. L.; Steendam, R. R. E.; Gerard, C. J. J.; Haw, M. D.; Sefcik, J.; ter Horst, J. H. The Unexpected Dominance of Secondary over Primary Nucleation. *Faraday Discuss.* **2022**, *235*, 2166−2179.
(24) Forsyth, C.; Burns, I. S.; Mulheran, P. A.; Sefcik, J. Scaling of Glycine Nucleation Kinetics with Shear Rate and Glass-Liquid Interfacial Area. *Cryst. Growth Des.* **2016**, *16* (1), 136−144.
(25) Liu, J.; Svärd, M.; Rasmuson, Å. C. Influence of Agitation and Fluid Shear on Nucleation of m-Hydroxybenzoic Acid Polymorphs. *Cryst. Growth Des.* **2014**, *14*, 5521−5531.
(26) Debuysschère, R.; Rimez, B.; Zaccone, A.; Scheid, B. Experimental and Theoretical Investigation of Nonclassical Shear-Induced Nucleation Mechanism for Small Molecule. *Cryst. Growth Des.* **2023**, *23* (7), 4979−4989.
(27) Devos, C.; Xiouras, C.; Van Gerven, T.; Kuhn, S. Unraveling the Role of Fluid Shear on Primary Nucleation of Paracetamol through an Energy-Dissipation Rate Analysis. *Cryst. Growth Des.* **2024**, *24* (7), 2713−2723.
(28) Vesga, M. J.; McKechnie, D.; Mulheran, P. A.; Johnston, K.; Sefcik, J. Conundrum of γ Glycine Nucleation Revisited: To Stir or Not to Stir? *CrystEngComm* **2019**, *21* (21), 2234−2243.
(29) McKechnie, D.; Mulheran, P. A.; Sefcik, J.; Johnston, K. Tuning Interfacial Concentration Enhancement through Dispersion Interactions to Facilitate Heterogeneous Nucleation. *J. Phys. Chem. C* **2022**, *126* (38), 16387−16400.
(30) Little, L. J.; Sear, R. P.; Keddie, J. L. Does the γ Polymorph of Glycine Nucleate Faster? A Quantitative Study of Nucleation from Aqueous Solution. *Cryst. Growth Des.* **2015**, *15*, 5345−5354.
(31) Kubota, N.; Kubota, K. Secondary Nucleation of Magnesium Sulphate from Single Seed Crystal by Fluid Shear in Agitated Supersaturated Aqueous Solution. *J. Cryst. Growth* **1986**, *76* (1), 69−74.
(32) Wang, J.; Estrin, J. Secondary Nucleation of Sucrose by Fluid Shear in Aqueous Solutions. *Chem. Eng. Commun.* **1996**, *152*−*153* (1), 275−286.
(33) Wang, M. L.; Yang, H. M. Secondary Nucleation of ∈-caprolactam in toluene solution by fluid shear forces. *Chem. Eng. Commun.* **1981**, *12* (4−6), 241−251.
(34) Mersmann, A. *Crystallization Technology Handbook*, 2nd ed.; Boca Raton: CRC Press, 2001.
(35) Tung, H.-H.; Paul, E. L.; Midler, M.; McCauley, J. A. *Crystallization of Organic Compounds: An Industrial Perspective*, 2nd ed.; Wiley, 2023.
(36) Tyrrell, R.; De Souza, B.; Frawley, P. J. Particle Breakage: Limiting Conditions for Crystal-Crystallizer Collisions. *Cryst. Growth Des.* **2018**, *18*, 617−622.
(37) O'Regan, S.; Frawley, P. J.; Shardt, O. The Effects of Particle Shape, Orientation, and Reynolds Number on Particle-Wall Collisions. *Comput. Fluids* **2023**, *266*, No. 106053.
(38) Kitamura, M.; Hayashi, Y. Secondary Nucleation Behaviour and the Mechanism in Antisolvent Crystallization of Thiazole Derivative Polymorphs. *Ind. Eng. Chem. Res.* **2016**, *55* (5), 1413−1418.
(39) Anwar, J.; Khan, S.; Lindfors, L. Secondary Crystal Nucleation: Nuclei Breeding Factory Uncovered. *Angew. Chem., Int. Ed.* **2015**, *54* (54), 14681−14684.
(40) Bosetti, L.; Ahn, B.; Mazzotti, M. Secondary Nucleation by Interparticle Energies. I. Thermodynamics. *Cryst. Growth Des.* **2022**, *22* (1), 87−97.

https://doi.org/10.1021/acs.cgd.4c00130
Cryst. Growth Des. 2024, 24, 4975−4984